Ultrafast emission from colloidal nanocrystals under pulsed X-ray excitation

2016 JINST 11 P10015

(http://iopscience.iop.org/1748-0221/11/10/P10015)

Published by IOP Publishing for Sissa Medialab

Received: *June 21, 2016*
Revised: *September 26, 2016*
Accepted: *October 10, 2016*
Published: *October 19, 2016*

Ultrafast emission from colloidal nanocrystals under pulsed X-ray excitation

R.M. Turtos,[a] **S. Gundacker,**[d] **A. Polovitsyn,**[b,c] **S. Christodoulou,**[b,c] **M. Salomoni,**[a] **E. Auffray,**[d] **I. Moreels,**[b] **P. Lecoq**[d] **and J.Q. Grim**[e,1]

[a] *Università degli Studi di Milano Bicocca, Piazza dell'Ateneo Nuovo 1, 20126, Milano, Italy*
[b] *Istituto Italiano di Tecnologia, via Morego 30, IT-16163, Genova, Italy*
[c] *Department of Physics, University of Genoa, via Dodecaneso 33, IT-16146 Genova, Italy*
[d] *CERN, 1211 Geneve 23, Switzerland*
[e] *U.S. Naval Research Laboratory, Washington, DC 20375, U.S.A.*

E-mail: joel.grim@nrl.navy.mil

Abstract: Fast timing has emerged as a critical requirement for radiation detection in medical and high energy physics, motivating the search for scintillator materials with high light yield and fast time response. However, light emission rates from conventional scintillation mechanisms fundamentally limit the achievable time resolution, which is presently at least one order of magnitude slower than required for next-generation detectors. One solution to this challenge is to generate an intense prompt signal in response to ionizing radiation. In this paper, we present colloidal semiconductor nanocrystals (NCs) as promising prompt photon sources. We investigate two classes of NCs: two-dimensional CdSe nanoplatelets (NPLs) and spherical CdSe/CdS core/giant shell quantum dots (GS QDs). We demonstrate that the emission rates of these NCs under pulsed X-ray excitation are much faster than traditional mechanisms in bulk scintillators, i.e. 5d-4f transitions. CdSe NPLs have a sub-100 ps effective decay time of 77 ps and CdSe/CdS GS QDs exhibit a sub-ns value of 849 ps. Further, the respective CdSe NPL and CdSe/CdS GS QD X-ray excited photoluminescence have the emission characteristics of excitons (X) and multiexcitons (MX), with the MXs providing additional prospects for fast timing with substantially shorter lifetimes.

Keywords: Timing detectors; Hybrid detectors; Materials for solid-state detectors; Scintillators, scintillation and light emission processes (solid, gas and liquid scintillators)

[1] Corresponding author.

doi:10.1088/1748-0221/11/10/P10015

2016 JINST 11 P10015

Contents

2016 JINST 11 P10015

1 Introduction

Over the last few decades, radiation detector research has largely been directed toward the discovery and development of scintillators with improved energy resolution via increased light yield and better proportionality [1, 2]. More recently, generating a prompt response to the passage of ionizing particles has emerged as a critical requirement for next-generation radiation detectors, notably in high energy physics (HEP) and time-of-flight positron emission tomography (TOF-PET) applications [3]. In the search for rare events in the planned High Luminosity Large Hadron Collider (HL-LHC), for example, event discrimination will require a sub-20 ps time resolution to mitigate pile-up events produced by the high luminosity of particle bunches, i.e. $> 1 \times 10^{35}$ cm^{-2}s^{-1} [4]. Similarly, precise time-tagging of 511 keV $\gamma-$rays is required in TOF-PET in order to confine the annihilation point along the line of response (LOR) [5, 6], and improve the signal to noise ratio.

State-of-the-art coincidence time resolution (CTR) values on the order of 117 ± 3 ps have been achieved for 20 mm long LSO:Ce Ca co-doped crystals using 511 keV [7] $\gamma-$rays, which translates into a background rejection area of the order of a few centimeters. Reaching the millimeter level for vertex identification, however, necessitates CTR values of 10 ps or less. Reducing CTR values can be achieved via increasing the light yield, shortening scintillation signal rise and decay times, or introducing a strong prompt signal [3]. The intrinsic light yield measured for LYSO crystals is 40 000 Ph/MeV ± 10% (syst) ± 3% (stat) under minimum ionizing electron excitation [8] and the decay times in cerium doped systems are limited to 16ns [9]. This sets a limit to the improvement

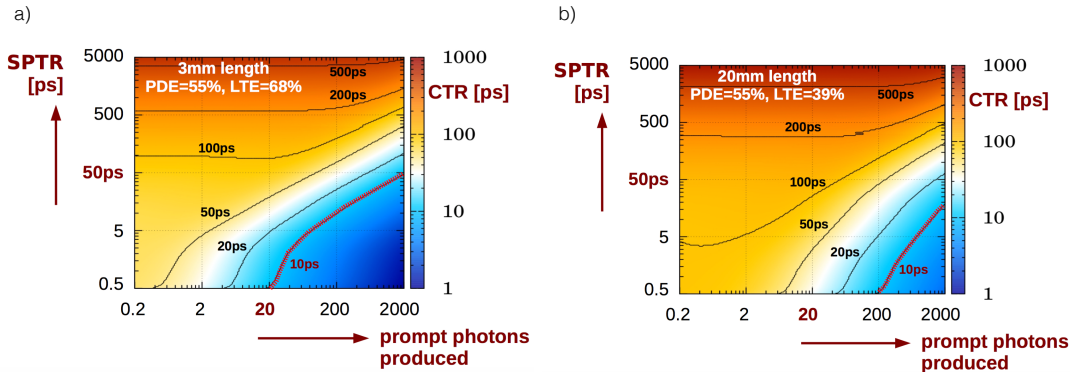

Figure 1. Cramèr-Rao lower bound calculations for CTR using a LSO:Ce scintillator of (a) 3 mm and (b) 20 mm length as function of SPTR and number of prompt photons.

that photostatistics can bring to CTR measurements, requiring that new approaches to achieving a prompt photo-response must be explored. Figure 1 presents Cràmer-Rao lower bound calculations for CTR values as a function of the single photon time resolution (SPTR expressed in sigma) and number of prompt photons produced along with the scintillation emission in the crystal. For the calculations shown, we used the time profile of LSO:Ce, i.e. scintillation rise time of τ_r = 70 ps and decay time of τ_d = 40 ns, and crystals of 3 mm and 20 mm lengths with different light transfer efficiencies (LTEs). As shown in ref. [3] and figure 1, a coincidence time resolution of 10 ps FWHM can be achieved with a prompt signal of several hundreds of photons provided that the SPTR of the SiPM is of the order of 10 ps sigma. Commercially available SiPMs do not provide this value, however, measurements performed on free standing single photon avalanche diodes of the SiPM showed SPTR values below 10 ps sigma. Consequently, SiPM engineering has to be improved together with light production mechanisms, as discussed in this paper, to reach CTR values of 10 ps.

Processes such as the Cerenkov effect [10–12] and hot-intraband emission [13, 14] have been investigated for this purpose, though both are low light yield processes. This motivates research not only towards ultrafast sub-nanosecond performance but also to materials that have the potential to produce prompt photons with sufficiently high yield under ionizing irradiation.

Here, we present ultrafast emission dynamics of colloidal semiconductor nanocrystals (NCs) as a new approach for prompt photon generation. In figure 2, the fast rise and decay for CdSe nanoplatelets (NPLs) and CdSe/CdS giant shell quantum dots (GS QDs) contrasted with the slower dynamics of LSO:Ce under pulsed X-ray excitation provides clear motivation for this work. CdSe NPLs are solution-processed quantum wells that are characterized by strong quantum confinement in only one dimension. Weak confinement in the lateral dimensions has two important consequences. First, in contrast to spherical NCs, momentum conservation rules apply more strictly, which reduces accessible states for Auger transitions. Second, a collective phasing of dipoles over many unit cells permits a giant oscillator strength transition (GOST) [15–17], resulting in ultrafast emission rates. We also investigate spherical GS QDs. In addition to better photostability compared to the core-only CdSe NPLs, their reduced emission/absorption band overlap (see figure 3(b)) will be advantageous in real devices where light has to potentially travel through at least 20 mm of material before it is detected.

2016 JINST 11 P10015

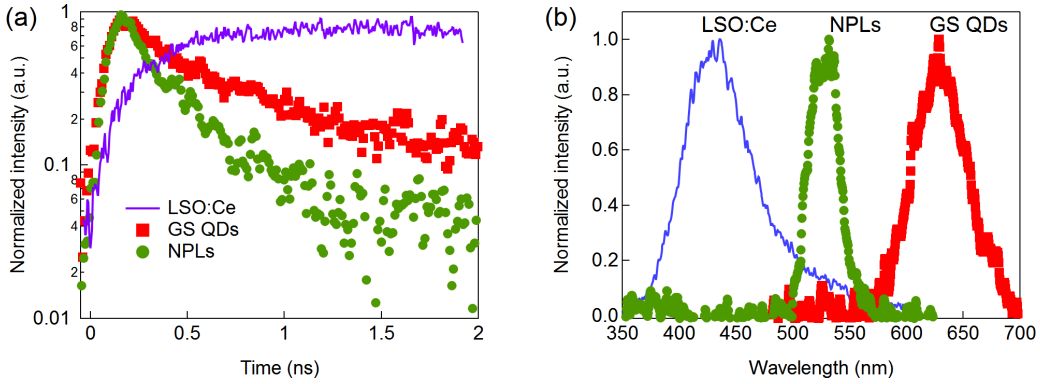

Figure 2. (a) Time-resolved photoluminescence and (b) steady-state spectra for LSO:Ce, CdSe/CdS GS QDs, and CdSe NPLs under pulsed X-ray excitation.

The tunable optoelectronic properties of NCs combined with recent advances in controlling their size, shape, core/shell heterostructure, and surface chemistry have enabled their use in a wide range of photonic applications. They have shown particular promise for bio-labeling [18], low-threshold lasing [17, 19, 20], photovoltaics [21], and single photon sources for quantum information [22, 23]. The high quantum yields (QYs) of NC quantum dots (QDs) has also generated interest in their use as low-cost, high-resolution scintillators for radiation detection [24–26]. Toward this end, the response of QDs under high energy electron [27], alpha [28], soft X-ray [29] and γ-ray [30] irradiation has been investigated. Initial high energy excitation studies have highlighted several important challenges that all degrade the light emitting properties of NCs, notably nonradiative Auger recombination [27], photo-instability [31], and losses due to the reabsorption of emitted light [30]. These challenges arise from the nature of NCs as small $\lesssim$100 nm semiconductors. On this size scale, strong carrier confinement results in efficient Auger recombination, high surface to volume ratios makes them sensitive to the external environment and damage, and small Stokes shifts result in significant reabsorption of emitted light. All of these issues degrade the performance of scintillators. For instance, nonlinear quenching such as Auger recombination that occurs at the high carrier densities created at electron track ends has been identified as a major cause of scintillator nonproportionality [9, 32, 33], and therefore degraded energy resolution.

Fortunately, significant effort has been devoted to overcoming these barriers to advance the development of NCs for the photonic applications mentioned above. Auger recombination, for example, has been mitigated with 2D nanoplatelets (NPLs) [17, 34] and heterostructured core/shell NCs [35]. Similarly, CdSe/CdS core/shell and particularly core/giant shell QDs (GS QDs) have improved photostability due to reduced charge transfer to deep, nonradiative surface traps. Further, reabsorption can be circumvented by engineering large Stokes shifts in GS QDs, where emission from a CdSe QD core and absorption from the larger band gap CdS shell are well-separated [21, 35].

2 Materials and methods

Details of the synthesis for the NPLs and GS QDs can be found in ref. [17] and ref. [36], respectively. The absorption and emission spectra and illustrations of the CdSe NPLs and CdSe/CdS GS QDs used in this work are shown in figure 3. These spectra are typical of these NCs, and depict several

2016 JINST 11 P10015

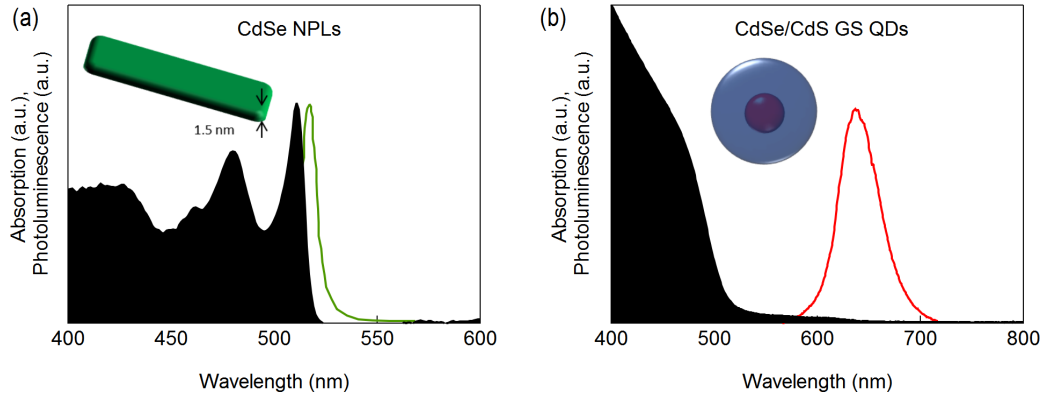

Figure 3. Absorption (black) and photoluminescence (green and red) spectra for (a) CdSe NPLs and (b) CdSe/CdS GS QDs.

of the characteristic features discussed above. For both CdSe NPLs and CdSe/CdS GS QDs, thin films were prepared by drop-casting from O.D. 30 toluene solutions.

The schematic of the experimental set up used to measure time-resolved laser and X-ray excited emission is shown in figure 4. Pulsed X-rays with energies up to 40 keV were generated with a repetition rate of 4 MHz by a picosecond diode laser PiLAS at 372 nm. Samples were mounted a few millimeters from the X-ray window of a Hamamatsu N5084 X-ray tube. The resulting photoluminescence was spectrally dispersed with a 50 gr/mm grating in a Spectrograph 2300i spectrometer. These photons were subsequently converted to photoelectrons and deflected in a C10910 Hamamatsu streak camera, which was operated in single photon counting mode. A typical streak image obtained when exciting a CdSe NPL thin film with X-rays is shown in figure 4, with time increasing downward along the vertical axis and photon wavelength increasing to the right along the horizontal axis. The spectral resolution is partly determined by a 500 μm spectrograph slit which results in a spectrally broadened spectrum. Additionally, the laser line under these conditions appears red-shifted by about 10 nm.

The total instrument response function (IRF) of the system was determined by measuring the temporal profile of the laser under the same measurement settings, i.e. sweeping range, optical path, and photocathode slit aperture. For a 100 μm slit aperture and 5 ns sweep range it is a Gaussian of 126 ps FWHM. The final IRF is the result of convolving the asymmetric tube time response (FWHM of 40 ps) with the laser response, resulting in an IRF of 134 ps FWHM. The total IRF was used to analyse X-ray excite data is the convolution of the laser IRF and the X-ray IRF. As can be seen in the decay of CdSe NPLs in figure 4(b), the first component of the CdSe NPL decay is resolution limited. Data is shown in figure 4(a) where the CdSe emission is centered at 530 nm due to multiexciton (MX) generation. In the case of a 2 ns sweeping range, the laser IRF reduces to 63 ps FWHM, and the total IRF has a FWHM of 74 ps.

Measurements were done in single photon counting mode and calibrated by sweeping range non-linearities. Both the 372 nm laser and X-ray excitation were used to excite thin films of the NCs, which were deposited on glass and on the surface of conventional bulk scintillators. Two different fit procedures were used depending on laser or X-ray excitation (laser IRF or total IRF). The laser-excited results were analyzed with the following formula [3] where the convolution using

2016 JINST 11 P10015

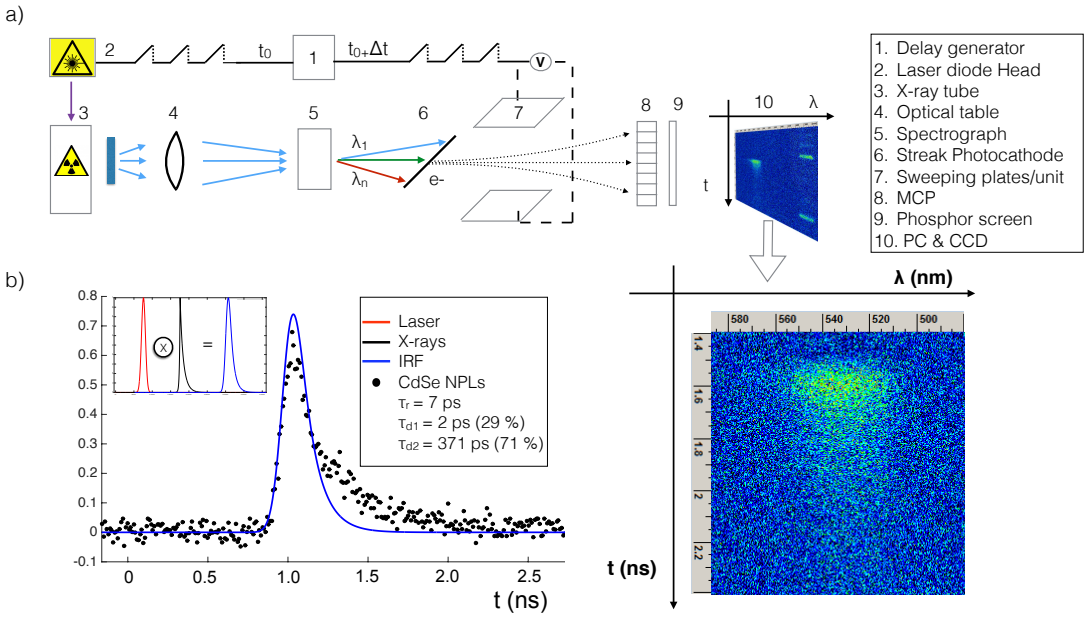

Figure 4. Schematic view of the primary components of the experimental setup. (a) Streak camera image of a CdSe nanoplatelets sample deposited on glass measured under X-rays excitation with a sweeping time of 2 ns. (b) Determination of the system IRF for 100 μm photocathode aperture and 5ns sweeping range, shown along with the decay of the CdSe NPL emission.

the laser IRF is done analytically:

$$F(t) = \sum_{i}^{N} \frac{y_i}{\tau_{d,i} - \tau_{r,i}} \cdot \exp^{\frac{2\tau_{d,i}(\theta - t) + \sigma^2_{\mathrm{IRF}}}{2\tau^2_{d,i}}} \cdot \left(1 - erf\left[\frac{\tau_{d,i}(\theta - t) + \sigma^2_{\mathrm{IRF}}}{\sqrt{2}\sigma_{\mathrm{IRF}} \cdot \tau_{d,i}}\right]\right)$$
$$- \sum_{i}^{N} \frac{y_i}{\tau_{d,i} - \tau_{r,i}} \cdot \exp^{\frac{2\tau_{r,i}(\theta - t) + \sigma^2_{\mathrm{IRF}}}{2\tau^2_{r,i}}} \cdot \left(1 - erf\left[\frac{\tau_{r,i}(\theta - t) + \sigma^2_{\mathrm{IRF}}}{\sqrt{2}\sigma_{\mathrm{IRF}} \cdot \tau_{r,i}}\right]\right) + C \qquad (2.1)$$

Here, θ describes the start of the emission process and the electronic delay. The term C accounts for the background coming from the MCP noise. The sum stands for the number of components characterizing rise and decay times.

For X-ray excited data, a fast Fourier transform convolution is done by building up a probability density function as a model to fit the data. Parameter errors are calculated using the Minos algorithm. The function used to convolve with the asymmetric IRF is the following [3]:

$$f(t) = \sum_{i}^{N} \frac{y_i}{\tau_{d,i} - \tau_{r,i}} \cdot \exp^{\frac{(\theta - t)}{\tau_{d,i}}} - \sum_{i}^{N} \frac{y_i}{\tau_{d,i} - \tau_{r,i}} \cdot \exp^{\frac{(\theta - t)}{\tau_{r,i}}} \qquad (2.2)$$

Both functions are normalized to the total photon yield, therefore y_i represents the abundance of each component in terms of photons emitted. In order to minimize the degrees of freedom, the rise time for different components is set as one parameter, since the resolution does not allow a proper estimation of recombination times smaller than 18 ps. For both analyses, the fractional weights are calculated as $Y_i = y_i / \sum_i y_i$, which is the percentage of photons emitted with a lifetime component τ_i.

2016 JINST 11 P10015

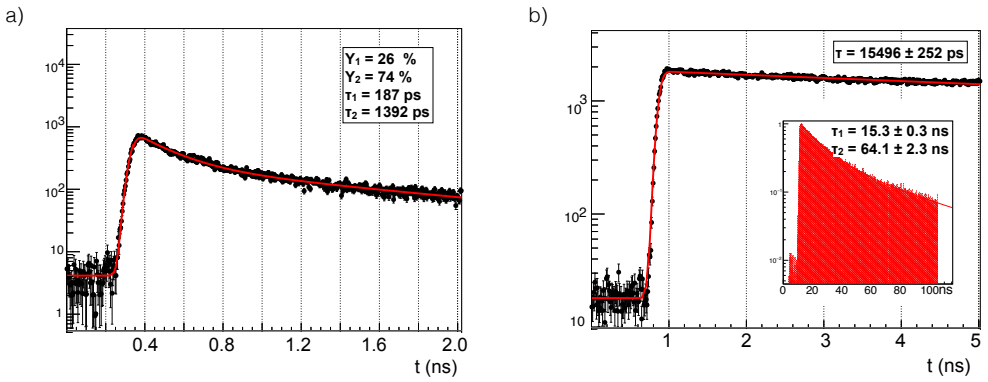

Figure 5. Nanocrystals timing performance under pulsed 372 nm laser excitation. (a) CdSe NPLs. (b) CdSe/CdS GS QDs.

3 Results

3.1 Laser excitation of NC thin films

The 372 nm picosecond laser used to trigger X-rays was used to excite the NC films on a glass substrate. The sweeping range for the laser excited measurements was chosen to be the same that for X-rays excitation, together with slit aperture and laser settings. This guarantees the same laser IRF for both sets of measurements which allows us to make comparisons between laser and X-ray excited emission dynamics. A 2 ns gate was chosen for the CdSe NPLs for better resolution of the fast components. Meanwhile for GS QDs, the gate is open up to 5 ns since they present slower emission rates.

Timing performance under laser excitation from NPLs and QDs is shown in figure 5. The results for NPLs point toward excitonic emission, consistent with laser excitation studies performed using similar materials in reference [17]. Measurements of GS QDs PL within a 100 ns gate are shown as inset of figure 5(b), where two decay components with lifetimes of 15 ns and 64 ns, respectively, are required to fit the data. The 15 ns decay dominates the signal when a smaller window of 5 ns is used (figure 5(b)). These slow and fast components are consistent with the exciton and biexciton emission demonstrated in ref. [36].

3.2 X-ray excitation of NC thin films

3.2.1 CdSe nanoplatelets

As described in Materials and Methods above, close-packed NC thin films were prepared by sequential drops from toluene solutions onto 100 μm glass coverslips. The CdSe NPL film thickness was roughly 11 μm, determined from the solution concentration, volume deposited, and film area. The streak image in figure 6(a) shows the time-resolved emission spectrum centered at about 530 nm of CdSe NPLs under X-ray excitation. Figure 6(c) shows that this spectrum is red-shifted compared to low-intensity laser excitation, which is consistent with biexciton (XX) or multiexciton (MX) emission. Both spectra are broad compared to the spectrum shown in figure 3 since they were taken with a 500 μm spectrometer entrance slit to improve light collection.

2016 JINST 11 P10015

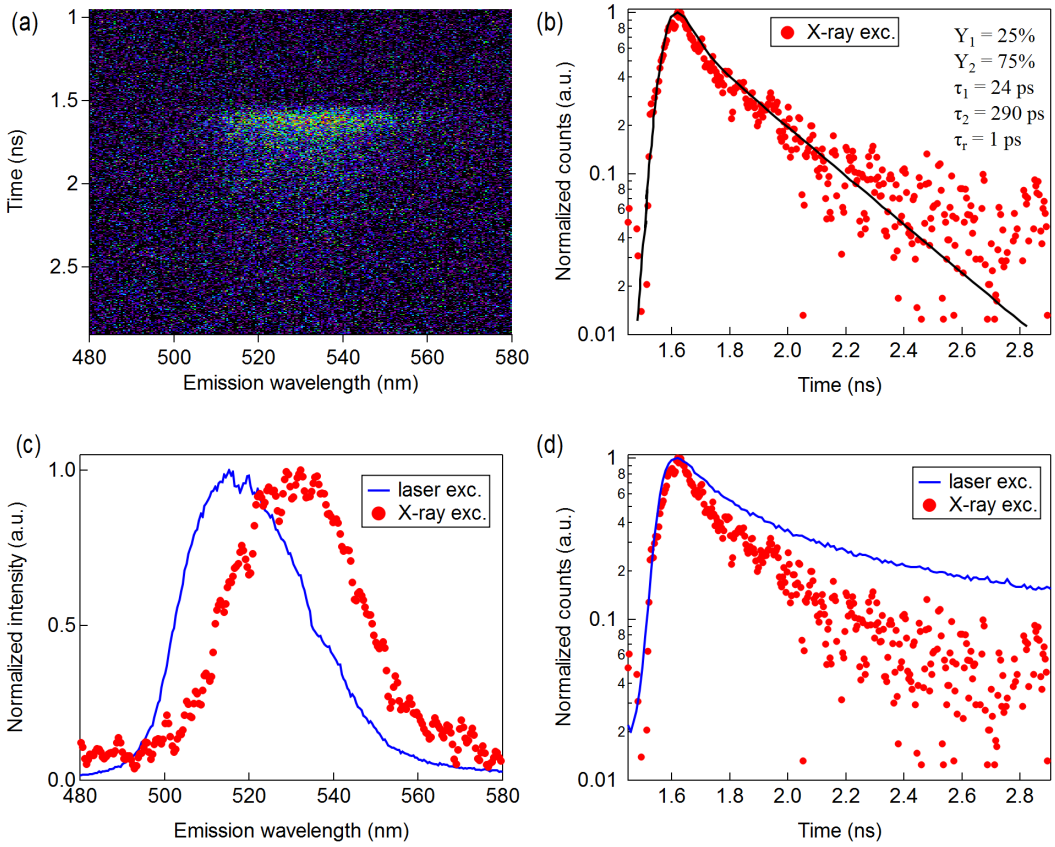

Figure 6. X-ray excitation of a CdSe NPL film on glass. (a) Streak image showing the X-ray excited CdSe NPL time-resolved emission spectrum. (b) Spectral integration of the full signal shown in panel (a). (c) X-ray excited spectrum compared to the spectrum obtained under low intensity laser excitation. Spectra were obtained by temporal integration of the respective streak camera images. A 500 μm spectrometer entrance slit was used in both cases. (d) Comparison of the X-ray and laser excited PL time dynamics. Together, (c) and (d) indicate significant biexciton or multiexciton emission under X-ray excitation.

Further evidence of XX/MX emission is provided by comparing the X-ray and laser excited emission rates in figure 6(d). Under low-intensity laser excitation, the effective lifetime of 520 ps is indicative of purely excitonic emission. Conversely, a significant portion of the energy from 40 keV X-ray excitation will be deposited in dense clusters, exciting multiple carriers in each NPL, which results in the observed fast, spectrally shifted XX/MX emission.

3.2.2 CdSe/CdS giant shell quantum dots

As mentioned above, GS QDs have several features that make them a promising material class for radiation detection. Importantly, the large CdS shell reduces carrier losses due to defect trapping by passivating traps on the CdSe surface and providing separation from the external environment. This results in both high quantum yields and enhanced photostability compared to core-only or thin shell QDs. An undesirable consequence of the CdS shell for the present work is a reduced oscillator strength due to electron delocalization in the CdS shell and hole confinement in the CdSe core. This

2016 JINST 11 P10015

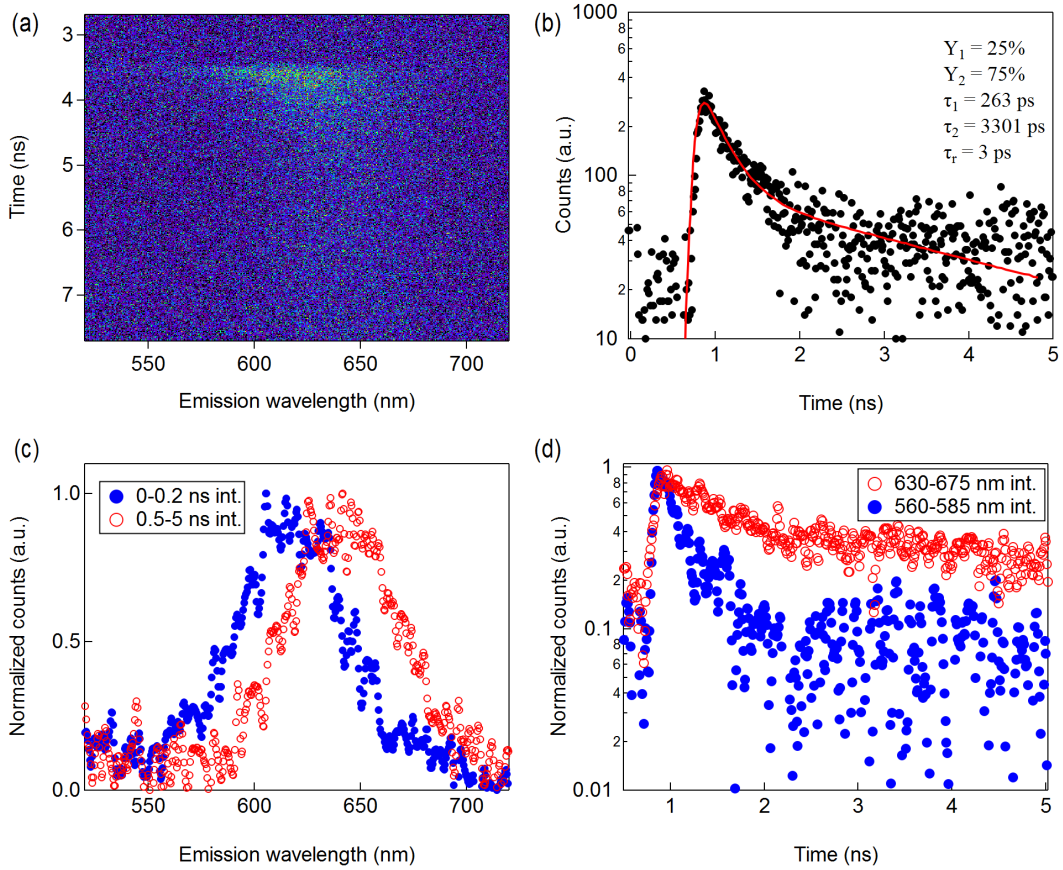

Figure 7. X-ray excitation of CdSe/CdS GS QDs film. (a) Streak image showing the GS QDs time-resolved emission spectrum. (b) Spectral integration of the full signal shown in panel (a). (c) Early time (0–0.2 ns) and later time (0.5–5 ns) spectra reveals a blue-shifted spectrum at early times. (d) Spectral integration of narrower slices on the red and blue side of GS QDs emission peak in panel (a). Together, (c) and (d) point toward multiexciton generation under X-ray excitation.

results in the radiative lifetime increasing with shell thickness [36], and longer lifetimes than CdSe NPLs (see figure 5).

However, similar to the CdSe NPLs above, the results shown in figure 7 demonstrate faster emission dynamics under X-ray excitation than under low intensity laser excitation. Possible sources of these faster dynamics can be excited state [37] and MX recombination, both of which are characteristically blue shifted for QDs. Auger recombination in the XX population could also play a role in shortening the lifetime. Examining the streak image in figure 7(a) confirms these possibilities, with the faster dynamics occurring on the blue side of the emission spectrum (figure 7(d). The blue shift also excludes the possibility that the fast lifetimes in GS QDs are due to sample heating, which would be characterized by a red-shifted spectrum. Further, the 82 meV blue shift of the early time spectrum points toward higher order MX generation beyond biexcitons [38].

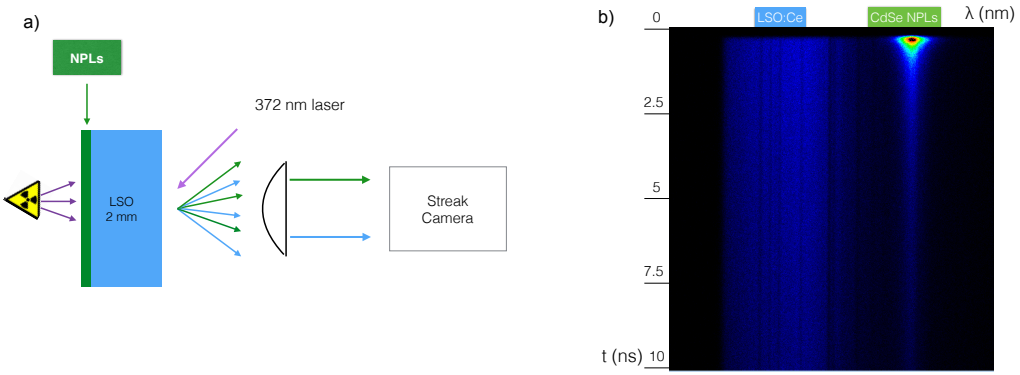

Figure 8. (a) Schematic view of the setup used to measure the heterostructure emission using laser and X-ray excitation. (b) NPLs/LSO:Ce system under laser excitation.

3.3 Nanocrystal and bulk scintillator heterostructures

Building up the thickness of NC films to fully stop high energy particles is challenging. One solution is to construct hybrid NC-bulk materials. In this approach, NCs can be used for the specialized task of fast timing while the bulk scintillator provides stopping power and scintillation light for tasks such as resolving particle energy. Such a detector could be constructed from stacks of thin wafers of bulk scintillators with films of NCs coating their surfaces. The design of this heterostructure for fast γ-ray tagging, for example, could be accomplished by making the dense bulk scintillator layer thinner than the recoil electron range, allowing energy transfer to the nanocrystal thin film [39]. In the following sections, we investigate this concept by depositing CdSe NPL films and GS QD films on the surfaces of LSO:Ce and LuAG:Ce, respectively. In this way, photoluminescence coming from NCs and conventional scintillators can be spectrally resolved in one streak image, which allows the efficiency of the NCs to be estimated by comparing to known light yield values of the bulk scintillators. A schematic view of the measurement can be seen in figure 8 together with a streak image taken under laser excitation with the NPL heterostructure.

3.3.1 CdSe NPLs deposited on LSO:Ce

A thin film of CdSe NPL was deposited on one of the large faces of a $2\times6\times8$ mm^3 LSO:Ce crystal. X-rays directly excite the NPLs film and the energy that has not been deposited in the NCs then reaches the scintillator along the 2 mm long axis. Light imaged from a $500\mu m \times 100\,\mu$m spot is shown in figure 9(a), where ultrafast CdSe NPL emission is seen between 505–550 nm, spectrally shifted from the LSO:Ce photoluminescence. The sweeping range was set to 2 ns, which allows us to resolve the first NPL decay component and directly compare to the intrinsic dynamics of NPLs presented in the previous section. A long tail which follows the LSO:Ce decay time characteristics is also present due to LSO:Ce blue light absorbed and re-emitted as green light from the CdSe NPLs. However, the majority of the CdSe NPL emission occurs during the LSO:Ce rise time.

3.3.2 CdSe/CdS GS QDs deposited on LuAG:Ce

A CdSe/CdS GS QDs film was deposited on the large face of a $1\times5\times5$ mm^3 LuAG:Ce crystal. The film was placed in front of the X-ray tube window and the sample was measured in transmission

2016 JINST 11 P10015

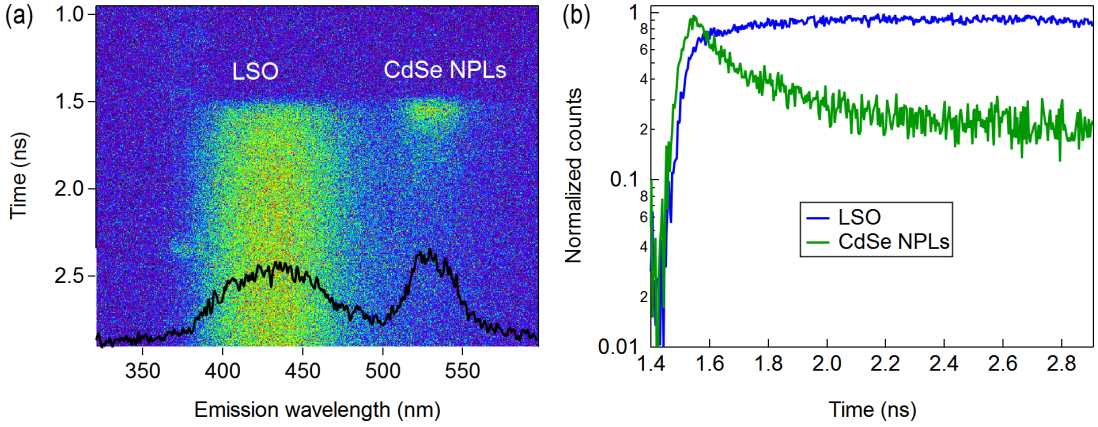

Figure 9. X-ray excitation of CdSe NPLs film deposited on a $2 \times 6 \times 8\,\mathrm{mm}^3$ LSO:Ce scintillating crystal. (a) Spectrally resolved streak image sweeping at 2 ns. (b) Spectral integration of the streak image to yield the decay traces for LSO:Ce and CdSe NPLs. The black line in (a) denotes the time-integrated profile.

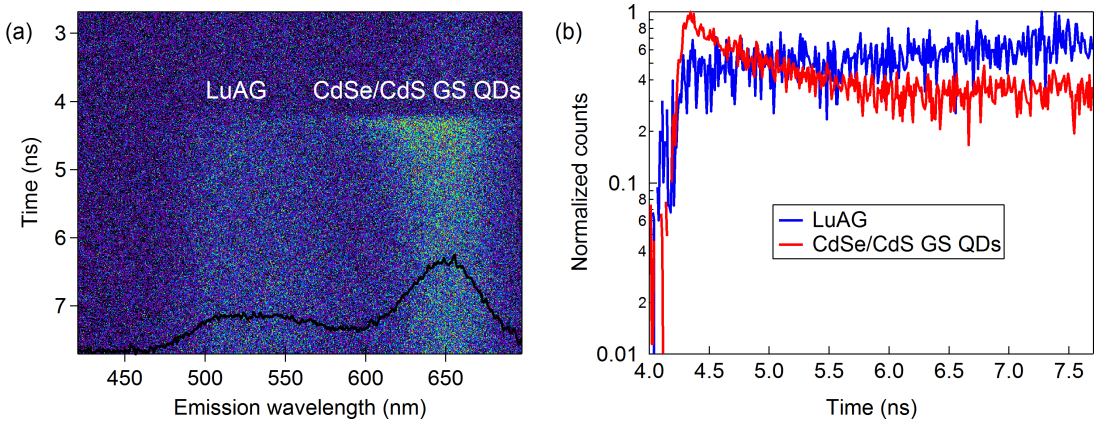

Figure 10. X-ray excitation of CdSe/CdS GS QDs film deposited on 1×5×5 mm^3 LuAG:Ce scintillating crystal. (a) Spectrally resolved streak image sweeping at 5 ns. (b) Timing performance of LuAG:Ce and GS QDs emission. The black line in (a) denotes the time-integrated profile.

mode through the 1 mm long axis. Light was collected from a $500\mu m \times 100\,\mu$m spot and both scintillation (LuAG:Ce) and ultrafast (QDs) emission are produced, which is shown in figure 10(a). There is a very fast QD component that occurs during the 500 ps rise time of the LuAG:Ce scintillation and a long tail which can be due to either the slow component seen in CdSe/CdS GS QDs [36], or absorption of LuAG:Ce light which is re-emitted with the typical LuAG:Ce decay characteristics.

3.4 NCs light yield estimations

The light yield of the NC films under X-ray excitation can be estimated by comparing to the LSO:Ce and LuAG:Ce emission in figure 9(a) and figure 10(a), respectively. Simulations using Geant4 [40] were used to determine the X-ray energy spectrum of the tungsten tube as well as the total energy deposited in the NC layer and scintillator after X-ray irradiation. To demonstrate the effect of the NC film thickness, simulations were run for thicknesses ranging from 100 nm to 100 μm. In the

2016 JINST 11 P10015

simulations, the NC films are declared using a filling factor of 50 % to account for the presence of organic surface ligands, which decreases the overall density of the film. The total number of photons emitted by the heterostructure is proportional to the energy deposited in each material and follows the relation:

$$\mathrm{LY}_{\mathrm{NPLs}} = \frac{\alpha_{\mathrm{NPLs}}}{Y_{200\mathrm{ps}}} * \mathrm{LY}_{\mathrm{LSO}}|_{t=1.5\mathrm{ns}} \frac{E_{\mathrm{dep}}^{\mathrm{LSO}}}{E_{\mathrm{dep}}^{\mathrm{NPLs}}} \tag{3.1}$$

$$\mathrm{LY}_{\mathrm{QDs}} = \frac{\alpha_{\mathrm{QDs}}}{Y_{300\mathrm{ps}}} * \mathrm{LY}_{\mathrm{LuAG}}|_{t=3.5\mathrm{ns}} \frac{E_{\mathrm{dep}}^{\mathrm{LuAG}}}{E_{\mathrm{dep}}^{\mathrm{QDs}}} \tag{3.2}$$

Here, α is the ratio between the total number of photons emitted by the NCs and the bulk scintillator. This ratio is taken from the integrated time profile. Since a rigorous calculation will have to account for the amount of light reabsorbed and emitted by the NCs, the estimations are done by taking the number of photons emitted at early times of 0 to 200 ps for NPLs and 0 to 300 ps for GS QDs, and normalizing to the total light yield with $Y_{200\mathrm{ps}} = 0.61$ and $Y_{300\mathrm{ps}} = 0.23$, respectively. For this correction, the timing dynamics of the NCs on glass under X-ray excitation are used. The relative wavelength dependence of the streak photocathode quantum efficiency and the efficiency of the spectrograph grating are also taken into account. Doing a background correction and comparing integrals of blue and green light, we calculate $\alpha_{\mathrm{NPLs}} = 0.1$ for the green photons emitted between 0 and 200 ps. In the case of QDs/LuAG, $\alpha_{\mathrm{QDs}} = 1$ for red photons emitted between 0 and 300 ps.

Considering the LSO intrinsic light yield as 40 000 ph/MeV, the amount of light emitted in the first 1.5 ns will be $\sim$ 1500 ph/MeV, represented by the term $LY_{\mathrm{LSO}}|_t$. In the case of GS QDs/LuAG, we have taken an intrinsic light yield of 23 000 ph/MeV based on comparative light yield measurements [7]. Since LuAG:Ce has a second decay tail up to 1063 ns and the repetition rate is 250 ns, the $LY_{\mathrm{LuAG}}|_t$ for $t < 3.5$ ns is approximately 500 ph/MeV. This calculation considers a rise time of 535 ps, and 2 decays components with different yields: 44%, 70 ns and 56%, 1063 ns taken from [3].

The computed mean energy depositions are shown in figures 11(c) and 11(d), normalized to the value obtained for a 100 μm thick film.

Measuring the light yield for NC films under X-ray excitation is a challenging task, and is part of ongoing work. Some of the crucial requirements for this measurement are that the films must have a constant thickness and a known packing density. In the present work, NC films were prepared by drop-casting from toluene solutions since this technique enables building up relatively thick films with sequential, concentrated drops. However, the NC films prepared for this work had considerable variation in thickness. We estimated an average thickness on the order of 10 μm, determined from the solution concentration, volume deposited, and film area. This is a rough estimate, and does not account for the variation in film thickness. Using the average value of 10 μm, we calculate light yields of 2,500 and 22,000 photons/MeV for CdSe NPLs and CdSe/CdS GS QDs, respectively.

4 Discussion

The lifetimes, component yields, and fraction of light emitted in the first 10 ps and 100 ps for CdSe NPLs and CdSe/CdS GS QDs are summarized in table 1, where both the NPLs and GS QDs

2016 JINST 11 P10015

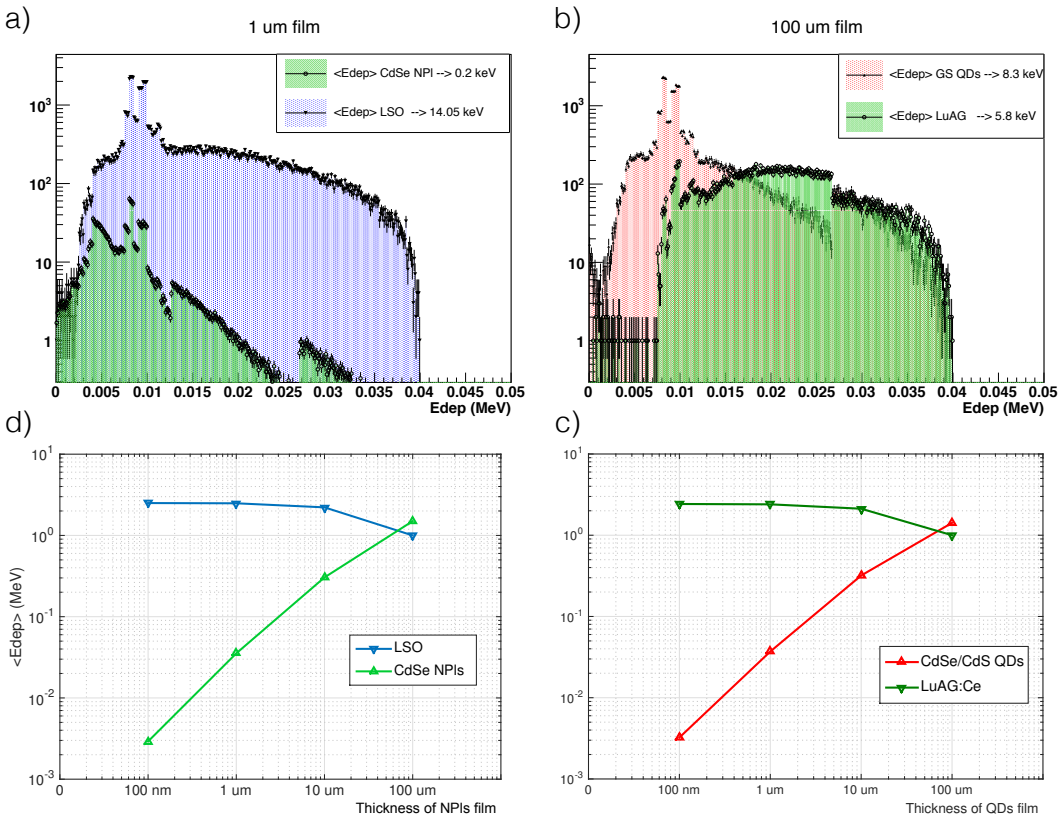

Figure 11. NC light yield estimations under 40 keV X-ray excitation as a function of film thickness. (a) Simulated spectrum of the energy deposited on NPLs/LSO heteroestructure for each material when the film thickness is 100 μm. (b) Spectrum of the energy deposited on QDs/LuAG heterostructure for each material when the film thickness is 100 μm obtained by simulations. c) and d) Values of mean energy deposited on NPLs/LSO and QDs/LuAG heterostructure for different film thickness.

have components in the lower sub-ns region. Under X-ray excitation, these fast components have larger relative amplitudes than under low-intensity laser excitation (see figure 5). The analysis done for the red and blue shifted emission coming from GS QDs is done using the laser IRF due to increased signal to noise in the narrower spectral slices. Since the fit using the laser IRF is done analytically instead of by numerical methods, it will introduce a better error estimation for low signal to noise data. Apart from the normalized yields for each decay component, an effective lifetime, $\tau_{\text{eff}} = \sum A_i \cdot \tau_i / \sum A_i$, is calculated for the different configurations using the amplitude of each component.

For CdSe NPLs, taking $\tau_{\text{eff}} = 520$ ps from low intensity laser excitation and $\tau_{\text{eff}} = 77$ ps from X-ray excitation (table 1), the ratio of the slower laser excited emission to the faster X-ray excited emission is 6.7. Considering that Auger recombination will typically lead to an order of magnitude or higher lifetime shortening [41], this indicates that it may not play a significant role in the fast emission dynamics of CdSe NPLs under X-ray excitation.

It is evident from the heterostructure results shown in figures 9 and 10 that an additional longer decay component emerges due to absorption of the bulk scintillator light by the NC films. This is

2016 JINST 11 P10015

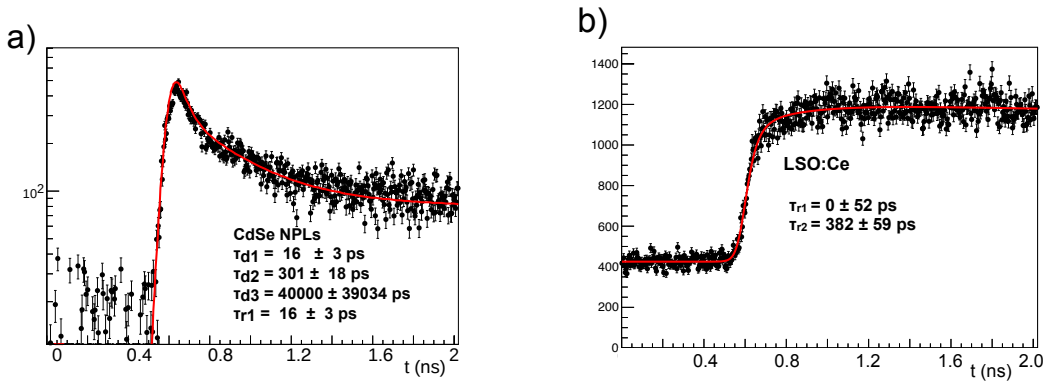

Figure 12. (a) Timing performance of the NPLs film when deposited on top of LSO:Ce. (b) Timing performance of a conventional scintillator, i.e. LSO:Ce in the first 1.5 ns.

Table 1. Summary of the laser and X-ray excited photoluminescence lifetimes with corresponding integrated photon yield fractions for NC thin films on glass substrates and on bulk scintillators. The effective lifetimes, $\tau_{\text{eff}} = \sum A_i \cdot \tau_i / \sum A_i$ were calculated using the respective amplitudes of each component. The GS QD results include lifetimes obtained for the slower red and faster blue sides of the spectrum, integrated over the spectral ranges shown in figure 7.

		laser IRF		total IRF	
NCs	Fits	$\text{NCs}_{\text{full}}^{\text{laser}}$		$\text{NCs}_{\text{full}}^{\text{x-rays}}$	$\text{Heter}_{\text{full}}^{\text{x-rays}}$
NPLs	τ_1	187 ± 910^{-4} ps		24 ± 8 ps	16 ± 3 ps
	Y_1	26%		25%	1%
	τ_2	1392 ± 110^{-4}ps		290 ± 11 ps	301 ± 18 ps
	Y_2	74%		75%	2%
	τ_{eff}	520 ps		77 ps	—
	Yield 10 ps	1.3%		7.6%	—
	Yield 100 ps	15%		44%	—
NCs	Fits	$\text{NCs}_{\text{red}}^{\text{x-rays}}$	$\text{NCs}_{\text{blue}}^{\text{x-rays}}$	$\text{NCs}_{\text{full}}^{\text{x-rays}}$	$\text{Heter}_{\text{full}}^{\text{x-rays}}$
GS QDs	τ_1	445 ± 45 ps	281 ± 18 ps	263 ± 25 ps	12 ps
	Y_1	18%	100%	25%	0.3%
	τ_2	3490 ± 321 ps	—	3301 ± 631 ps	763 ± 40 ps
	Y_2	82%	—	75%	1%
	τ_{eff}	1564 ps	281 ps	849 ps	—
	Yield 10 ps	0.7%	3.5%	0.8%	—
	Yield 100 ps	8.5%	30%	10%	—

shown in figure 12 for CdSe NPLs, where a long tail with a lifetime characteristic of the LSO:Ce decay time is present. However, the relative weights of the first and second decay components are preserved as shown in table 1. The third decay component is not shown since it follows the 40 ns and 100 ns decays of LSO:Ce and LuAG:Ce, respectively. This indicates negligible absorption/re-emission at early times (0–300 ps) of the scintillating pulse. Fitting the LSO:Ce

2016 JINST 11 P10015

rise time (figure 12(b)), the first two NPL decay components occur within the same timescale as the direct and delayed excitation of the Ce^{3+} luminescent centers, represented by τ_{r1} and τ_{r2}, respectively. Similarly, a long decay component following the LuAG emission lifetime appears for the GS QDs/LuAG heterostructure. In both cases, the secondary excitation by the bulk scintillator and the intrinsic longer lifetime components of the NCs can be reduced by isolating the fast MX emission via spectral filtering. This may serve as an important strategy when considering practical devices in which repeated layers of NC/bulk scintillators are involved. In such devices, eliminating longer lifetime components will enable faster cycle times (or frame rates).

5 Conclusion and outlook

We have demonstrated that a new generation of colloidal nanocrystals hold significant potential as a material class to generate a prompt photo-response to ionizing particles. NC radiative emission lifetimes are shown to be significantly shorter than traditional scintillation mechanisms. The CdSe nanoplatelets and giant shell quantum dots studied here overcome many of the challenges that earlier generations of NCs faced under ionizing radiation. Notably, nonradiative Auger recombination, which also deteriorates bulk scintillator performance, is suppressed in both systems. Further, the large shell of the CdSe/CdS GS QDs overcomes several other challenges, such as reabsorption of emitted light by separating emission and absorption bands. These features can in principle also be extended to NPLs via the growth of a larger bandgap shell such as CdS or ZnS.

Future studies of the ultrafast processes presented here will be aided by parallel efforts to lower the time resolution of the streak camera system when using X-ray excitation. The signal to noise ratio constitutes a major limitation, which can be overcome by increasing the X-ray flux in a 100 μm spot by means of a poly-capillary X-rays lens. The determination of the presently unresolved decay components for NPLs and QDs could bring deeper insight to faster regimes for light emission under ionizing radiation. Additionally, better determination of the NCs photon yield can be accomplished by using spin coating or an equivalent process of depositing uniform films of controllable thickness.

We have shown that colloidal nanocrystal-based scintillators are a promising approach to fast timing and provide a feasible path toward sub-20 ps time resolution. Future lines of research will be directed toward NCs embedded in a host matrix as proposed in ref. [26] in order to increase the stopping power and the energy transfer efficiency.

Acknowledgments

This work was carried out in the frame of the ERC Advanced Grant TICAL #338953 (PI Paul Lecoq) and the Crystal Clear collaboration. It was also supported by a Marie Curie Early Initial Training Network Fellowship of the European Community's 7^{th} Framework Programme under contract number (PITN-GA-2011-289355-PicoSEC-MCNet) and the COST Action Fast TD1401.

References

[1] C.W.E. van Eijk, *Inorganic scintillators in medical imaging*, *Phys. Med. Biol.* **47** (2002) R85.

2016 JINST 11 P10015

[2] P. Lecoq, *Development of new scintillators for medical applications*, *Nucl. Instrum. Meth.* **A 809** (2016) 130.

[3] S. Gundacker, E. Auffray, K. Pauwels and P. Lecoq, *Measurement of intrinsic rise times for various l(y)so and luag scintillators with a general study of prompt photons to achieve 10 ps in tof-pet*, *Phys. Med. Biol.* **61** (2016) 280.

[4] D. del Re, *Timing performance of the cms ecal and prospects for the future*, *J. Phys. Conf. Ser.* **587** (2015) 012003.

[5] S. Gundacker et al., *Time of flight positron emission tomography towards 100 ps resolution with l(y)so: an experimental and theoretical analysis*, 2013 *JINST* **8** P07014.

[6] E. Auffray et al., *Characterization studies of silicon photomultipliers and crystals matrices for a novel time of flight pet detector*, 2015 *JINST* **10** P06009.

[7] S. Gundacker and et al., *State-of-the-art timing in tof-pet detectors with luag, gagg and l(y)so scintillators of various sites coupled to fbk-sipms.*, 2016 *JINST* **11** P08008.

[8] R.M. Turtos et al., *Measurement of lyso intrinsic light yield using electron excitation*, *IEEE Trans. Nucl. Sci.* **63** (2016) 475.

[9] P. Dorenbos, *Fundamental limitations in the performance of Ce^{3+}, Pr^{3+}, and Eu^{2+} activated scintillators*, *IEEE Trans. Nucl. Sci.* **57** (2010) 1162.

[10] S.E. Brunner, L. Gruber, J. Marton, K. Suzuki and A. Hirtl, *Studies on the cherenkov effect for improved time resolution of tof-pet*, *IEEE Trans. Nucl. Sci.* **61** (2014) 443.

[11] S. Korpar, R. Dolenec, P. Križan, R. Pestotnik and A. Stanovnik, *Study of tof-pet using cherenkov light*, *Phys. Proc.* **37** (2012) 1531.

[12] P. Lecoq et al., *Factors influencing time resolution of scintillators and ways to improve them*, *IEEE Trans. Nucl. Sci.* **57** (2010) 2411.

[13] S. Omelkov, V. Nagirnyi, A. Vasil'ev and M. Kirm, *New features of hot intraband luminescence for fast timing*, *J. Luminesc.* **176** (2016) 309.

[14] P. Lecoq, M. Korzhik and A. Vasil'ev, *Can transient phenomena help improving time resolution in scintillators?*, *IEEE Trans. Nucl. Sci.* **61** (2014) 229.

[15] S. Ithurria et al., *Colloidal nanoplatelets with two-dimensional electronic structure.*, *Nature Mat.* **10** (2011) 936.

[16] A. Naeem, F. Masia, S. Christodoulou, I. Moreels, P. Borri and W. Langbein, *Giant exciton oscillator strength and radiatively limited dephasing in two-dimensional platelets*, *Phys. Rev.* **B 91** (2015) 121302.

[17] J.Q. Grim et al., *Continuous-wave biexciton lasing at room temperature using solution-processed quantum wells*, *Nature Nanotechnol.* **9** (2014) 891.

[18] D. Deng et al., *High-quality $CuInS_2$-ZnS quantum dots for in vitro and in vivo bioimaging*, *Chem. Mater.* **24** (2012) 3029.

[19] B. Guzelturk, Y. Kelestemur, M. Olutas, S. Delikanli and H.V. Demir, *Amplified spontaneous emission and lasing in colloidal nanoplatelets*, *ACS Nano* **8** (2014) 6599.

[20] V.I. Klimov et al., *Optical gain and stimulated emission in nanocrystal quantum dots*, *Science* **290** (2000) 314

[21] F. Meinardi et al., *Large-area luminescent solar concentrators based on stokes-shift-engineered nanocrystals in a mass-polymerized pmma matrix*, *Nature Phot.* **8** (2014) 392.

2016 JINST 11 P10015

[22] F. Pisanello et al., *Room temperature-dipolelike single photon source with a colloidal dot-in-rod*, *Appl. Phys. Lett.* **96** (2010) 033101.

[23] M.A.M. Versteegh et al., *Observation of strongly entangled photon pairs from a nanowire quantum dot*, *Nature Commun.* **5** (2014) 5298.

[24] L. Procházková, T. Gbur, V. Čuba, V. Jarý and M. Nikl, *Fabrication of highly efficient ZnO nanoscintillators*, *Opt. Mater.* **47** (2015) 67.

[25] C. Liu, T. J. Hajagos, D. Kishpaugh, Y. Jin, W. Hu, Q. Chen et al., *Facile single-precursor synthesis and surface modification of hafnium oxide nanoparticles for nanocomposite γ-ray scintillators*, *Adv. Funct. Mater.* **25** (2015) 4607.

[26] H. Burešová et al., *Preparation and luminescence properties of zno:ga polystyrene composite scintillator*, *Opt. Express* **24** (2016) 15289.

[27] L. A. Padilha, W. K. Bae, V. I. Klimov, J. M. Pietryga and R. D. Schaller, *Response of semiconductor nanocrystals to extremely energetic excitation*, *Nano Lett.* **13** (2013) 925.

[28] S. Létant and T. Wang, *Study of porous glass doped with quantum dots or laser dyes under alpha irradiation*, *Appl. Phys. Lett.* **88** (2005) 103110.

[29] P. Brůža et al., *Applications of a table-top time-resolved luminescence spectrometer with nanosecond soft x-ray pulse excitation*, *IEEE Trans. Nucl. Sci.* **61** (2014) 448.

[30] S.E. Létant and T. Wang, *Semiconductor quantum dot scintillation under γ-ray irradiation*, *Nano Lett.* **6** (2006) 2877.

[31] N.J. Withers et al., *Rapid degradation of cdse-zns colloidal quantum dots exposed to gamma irradiation*, *Appl. Phys. Lett.* **93** (2008) 173101.

[32] R.T. Williams et al., *Excitation density, diffusion-drift, and proportionality in scintillators*, *Phys. Stat. Sol.* **B 248** (2011) 426.

[33] J.Q. Grim et al., *Nonlinear quenching of densely excited states in wide-gap solids*, *Phys. Rev.* **B 87** (2013) 125117.

[34] L.T. Kunneman et al., *Bimolecular auger recombination of electron-hole pairs in two-dimensional cdse and cdse/cdzns core/shell nanoplatelets*, *J. Phys. Chem. Lett.* **4** (2013) 3574.

[35] F.G. Santamaría et al., *Suppressed auger recombination in giant nanocrystals boosts optical gain performance*, *Nano Lett.* **9** (2009) 3482.

[36] S. Christodoulou et al., *Synthesis of highly luminescent wurtzite cdse/cds giant-shell nanocrystals using a fast continuous injection route*, *J. Mater. Chem.* **C 2** (2014) 3439.

[37] G. Rainò et al., *Exciton dynamics within the band-edge manifold states: the onset of an acoustic phonon bottleneck*, *Nano Lett.* **12** (2012) 5224.

[38] H. Htoon et al., *Highly emissive multiexcitons in steady-state photoluminescence of individual giant cdse/cds core-shell nanocrystals*, *Nano Lett.* **10** (2010) 2401.

[39] P. Lecoq, *Metamaterials for novel x- or gamma-ray detector designs*, *IEEE Nucl. Sci. Symp. Conf. Rec.* **07-1** (2008) 680.

[40] S. Agostinelli and et al., *GEANT4 — A simulation toolkit*, *Nucl. Instrum. Meth.* **A 506** (2003) 250.

[41] C. Dang et al., *Red, green and blue lasing enabled by single-exciton gain in colloidal quantum dot films*, *Nature Nanotechol.* **7** (2012) 335.

2016 JINST 11 P10015